Tropospheric nitrogen dioxide levels vary diurnally in Asian cities

Junsung Park[1,2+], Hyunkee Hong[3+], Hanlim Lee[1*], Si-Wan Kim[4,5*], Jhoon Kim[4], Michel Van Roozendael[6], Caroline Fayt[6], Myong-Hwan Ahn[7], Daniel J. Jacob[8], Seunghwan Seo[4], Kyoung-Min Kim[4], Daewon Kim[1,9], Wonei Choi[1,10], Won-Jin Lee[3], Dong-Won Lee[3], Thomas Wagner[11], Andreas Richter[12], Nickolay A. Krotkov[13], Lok N. Lamsal[13,14,15], Dai Ho Ko[16], Seung Hoon Lee[16], Jung-Hun Woo[17]

[1]Division of Earth Environmental System Science, Major of Spatial Information Engineering, Pukyong National University, Busan, Republic of Korea
[2]Center for Astrophysics | Harvard & Smithsonian, Cambridge, Massachusetts, USA
[3]National Institute of Environmental Research, Incheon, Republic of Korea
[4]Department of Atmospheric Sciences, Yonsei University, Seoul, Republic of Korea
[5]Irreversible Climate Change Research Center, Yonsei University, Seoul, Republic of Korea
[6]Belgian Institute for Space Aeronomy (BIRA-IASB), Brussels, Belgium
[7]Department of Climate and Energy Systems Engineering/Social Economy, Ewha Womans University, Seoul, Republic of Korea
[8]Harvard School of Engineering and Applied Science, Harvard University, Cambridge, Massachusetts, USA
[9]Institute of Environmental Studies, Pusan National University, Busan, Republic of Korea
[10]NASA postdoctoral Program (NPP) at Goddard Space Flight Center, Greenbelt, Maryland, USA
[11]Max-Planck Institute for Chemistry (MPI-C), Mainz, Germany
[12]Institute of Environmental Physics (IUP-UB), University of Bremen, Bremen, Germany
[13]Atmospheric Chemistry and Dynamics Laboratory, NASA Goddard Space Flight Center, Greenbelt, Maryland, USA
[14]University of Maryland Baltimore County (UMBC), Baltimore, Maryland, USA
[15]Now at Bureau of Ocean Energy Management, Stirling, Virginia, USA
[16]Korea Aerospace Research Institute, Daejeon, Republic of Korea
[17]Department of Environmental Planning & Advanced Program for Urban Environmental Studies, Seoul National University

+Co-first author. These authors contributed equally to this work.
*Corresponding author: Hanlim Lee (hllee@pknu.ac.kr) and Si-Wan Kim (siwan.kim@yonsei.ac.kr)

Abstract

Satellite measurements of nitrogen dioxide have been used to infer nitrogen oxides emissions, a critical component in tropospheric chemistry and pollution. New observations from the Geostationary Environmental Monitoring Spectrometer offer a breakthrough by providing a daytime record of nitrogen dioxide over Asia. Here we present the summertime diurnal patterns of nitrogen dioxide at major cities, power plant regions, and Strait of Malacca. The Geostationary Environmental Monitoring Spectrometer data across various regions show high nitrogen dioxide in the morning that decrease in the afternoon, with varying hourly peaks, troughs, and amplitudes reflecting diurnal characteristics of local emissions and chemistry. Nitrogen oxides emissions inferred from Geostationary Environmental Monitoring Spectrometer and the Weather Research and Forecasting model coupled with Chemistry also show distinct patterns among regions: early morning peaks occur over Hanoi, Guangzhou, and Bangkok; mid-to-late morning peaks appear over Seoul and Beijing; and late afternoon peaks are noted in the Yangtze River Delta region. Top-down emissions incorporating temporal changes in the Geostationary Environmental Monitoring Spectrometer nitrogen dioxide yield the most accurate nitrogen dioxide simulations.

Introduction

NO_x (= NO + NO_2) is easily converted into nitrate aerosols and plays a key role in the formation of tropospheric ozone and acid rain[1]. Regular NO_2 monitoring with improved capabilities can help control NO_x emission levels. Near-surface concentrations of air pollutants, including NO_2, show variable diurnal changes depending on their source type and chemical and meteorological conditions[2]. Hourly tropospheric NO_2 monitoring afforded by space-borne Geostationary Earth Orbit (GEO) spectrometers promise to play a crucial role in next generation air quality monitoring. These GEO observations should have the benefit of diurnal estimating top–down NO_x emissions using more complete observations than based on twice–a–day measurements from Low Earth Orbit (LEO) sensors[3–5].

Over the past two decades, satellite data have revealed substantial regional variations in tropospheric NO_2 vertical column densities (VCDs) in industrial regions and cities worldwide. From 2000 to 2019, approximately 71% of urban regions experienced an increase in annual mean NO_2 concentrations, averaging +0.4% per year[6–7]. However, trends differed by region. North America and Europe showed notable declines in NO_2 levels, reflecting the impact of stringent air quality polices and emission reduction efforts[6–7]. In contrast, sub-Saharan Arica, the Middle East, and South Asia recorded increasing NO_2 concentrations, largely attributed to urban expansion and industrialization. Among these regions, South Asia recorded the highest NO_2 exposures, which remained largely constant over the past two decades despite regional variations. In this study, we refer to vertical column density (VCD) as simply "column". Although NO_2 columns in some Asian countries have declined in recent years, they tend to remain higher than those in Europe and North America[6–9]. However, many Asian countries have relatively few air quality sites that can continuously monitor NO_2 ambient concentrations. Until recently, this lack of spatial coverage of the surface monitoring networks has been

complemented by twice-a-day space-borne observations from LEO spectrometers such as Global Ozone Monitoring Experiment-2 (GOME-2) in the morning and Ozone Monitoring Instrument (OMI) and TROPOspheric Monitoring Instrument (TROPOMI) in early afternoon. This has recently changed with the launch of the two pioneering geostationary spectrometers: the Geostationary Environmental Monitoring Spectrometer (GEMS), which started hourly observations over Asia in 2020 and the Tropospheric Emissions: Monitoring Pollution (TEMPO) started hourly observations in 2023 over North America. The upcoming ESA/Copernicus Sentinel-4 geostationary spectrometer is planned for launch in 2025 for hourly observations over Europe and northern Africa.

Hyperspectral sensors on sun-synchronous polar-orbiting satellites have contributed substantially to identifying regional and global NO_2 spatial distribution characteristics and long-term trends, improving NO_x emissions estimates and elucidating atmospheric NO_x chemistry[10–18]. These instruments include the Global Ozone Monitoring Experiment (GOME[12]), the Global Ozone Monitoring Experiment-2 (GOME-2[13]), the SCanning Imaging Absorption spectroMeter for Atmospheric CHartographY (SCIAMACHY[14]), the Ozone Monitoring Instrument (OMI[15,16]), and the TROPOspheric Monitoring Instrument (TROPOMI[17]). These data have been retrieved twice–a–day (morning and early afternoon) from the constellation of LEO measurements[19]. However, the hourly daytime observations from GEO spectrometers such as GEMS and TEMPO facilitate investigating diurnal processes that determine the atmospheric composition[20–22]. In addition, top–down NO_x emissions have been estimated using tropospheric NO_2 column data available at limited times in the morning and/or afternoon from LEO measurements. When a single observation per day is available to infer emissions, it is necessary to assume that the existing knowledge of diurnal variations in chemistry and emissions are correct[23]. There is thus a need to evaluate previous assumptions about diurnal variations in NO_x emissions using tropospheric NO_2 data from geostationary

measurements. Studies have already examined the diurnal variations of observed NO_2 columns over limited regions using ground-based and airborne observations[24–26] as well as the constellation of LEO measurements[27,28]. These studies demonstrate diverse diurnal changes in column NO_2 concentrations, as well as a significant month-to-month and day-to-day variability in diurnal changes at a single site. These variations are collectively influenced by emissions, chemistry, and transport. Daytime spatial NO_2 distributions are now available, for the first time, at hourly resolution from Geostationary Environmental Monitoring Spectrometer (GEMS) observations. Detailed field of regard (FOR) and times of GEMS measurements are provided in Supplementary Fig. 1 and Supplementary Table 1. The unprecedented high spatiotemporal resolution of GEMS measurements can provide spatially complete information on diurnal variability in vertical column NO_2 densities over Asia, which is often lacking in both in-situ and remote-sensing observations.

Several papers regarding GEMS hourly data have been published recently[29–31]. One of them[29] was focused on understanding the diurnal variation in the GEMS tropospheric NO_2 column retrievals over Northeast Asia and Seoul in South Korea using a Multi-Scale Infrastructure for Chemistry and Aerosols (Version 0, MUSICAv0) 3D chemical transport model in January and June 2023. Another study[30] shows similar variability and diurnal variation of the NO_2 column in Beijing and Seoul using GEMS data, GEOS-Chem chemical transport model and ground-based Pandora observations. In addition, they examined the role of transport in the diurnal variation of NO_2 column. The other study[31] presents the correction for the operational GEMS L2 NO_2 columns using a machine learning model to train with TROPOMI NO_2 columns measured in early afternoon around 1:30 pm local solar time, because TROPOMI NO_2 retrievals are more mature. In addition, in the previous studies[32,33], the surface NO_2 concentration has been estimated using the GEMS L2 NO_2 product, and uncertainty has

been quantified. As presented in these studies the hourly data from GEMS can be used to gain new insights in diurnal evolution in atmospheric composition.

Herein, we identify the diurnal characteristics of tropospheric NO_2 column not only East Asia but also major cities and hotspots over Asia, where a considerable portion of global NO_x emissions occur. Three emissions source types are considered: cities, power plants, and ship tracks. This study focuses on the data collected during summer when the measurement data are available for a longer time interval of the day than in other seasons. Top-down NO_x emissions for each source are estimated utilizing a chemical transport model combined with GEMS observations. We also demonstrate the ability of GEMS to detect the transport of NO_2 plumes across South Korea within a single day.

Results and Discussion

Diurnal dependency of tropospheric NO_2 spatial distributions

To identify the dependency of the distribution on the time of the day, for the first time, we investigated diurnal cycles of multiple source regions over Asia as observed by GEMS for available times. We selected Seoul, Beijing, the Yangtze River Delta (including Shanghai), Guangzhou, Bangkok, and Hanoi as cities; power plant complexes in China named "Wuhai" and "Baotou" and clusters of power plants in India labeled "India P1", "India P2", and "India P3"; and one ship track region, the Strait of Malacca (see Fig. 1 and 2). In this study, in order to investigate the characteristics of diurnal variation in NO_2 column and estimate the NO_x emissions at hotspots over Asia, we focused on major cities and major hotspots that have huge anthropogenic source regions over GEMS field of regards. Some of major cities such as Tokyo were excluded due to insufficient observations. Locations of each source box and power plants, along with the number of GEMS data for each source, are detailed in Supplementary Tables 2-3 and Supplementary Figs. 3-6. Fig. 1 shows GEMS tropospheric NO_2 columns during weekdays and weekends for all source regions. The GEMS NO_2 values collected at a swath passing through a specific source box area with cloud fraction ≤ 0.3, solar zenith angle ≤ 70°, and viewing zenith angle ≤ 70° for summer of 2021 (June 1–August 31) and 2022 (June 1–August 31) are used to generate the mean and standard deviation. With the exception of Seoul, there are no significant differences in NO_2 columns between weekdays and weekends throughout the day across all source regions. A previous study indicated no significant weekday-weekend differences in satellite NO_2 columns in China[34]. In Seoul, there are large reductions in columns (up to 30%) on weekends compared to weekdays. There are some weekend NO_2 reductions observed in Bangkok and Hanoi (Fig. 1 and Supplementary Figs. 4-7).

In Fig. 1, the WRF-Chem NO_2 columns using constant NO_x emissions are compared with the GEMS columns to investigate how the satellite columns vary if there were no diurnal changes in the emissions. The model results were normalized to have the same average column values as the GEMS tropospheric columns for available times. Overall, the GEMS NO_2 columns show peaks in the morning, decrease after the peaks, and increase in the late afternoon in the cities (Fig. 1 and 2). The time of maximum in the morning ranges from 08:00 LT to 11:00 LT and the time of minimum in the afternoon varies from 13:00 LT to 16:00 LT. The minimum column values in the afternoon are 17% to 40% lower than the maximum values. Diurnal pattern of GEMS NO_2 and inferred NO_x emissions for each region is presented below.

- ***Seoul***

In Seoul, the average tropospheric NO_2 column was low in the early morning (08:00–09:00 LT), peaked in the late morning (11:00 LT), decreased in the early afternoon, and then started to increase again in the late afternoon (15:00 LT). The minimum GEMS column value in the afternoon is approximately 30% lower than the maximum value in the late morning. The WRF-Chem model results using a constant emission over Seoul exhibit different diurnal patterns, particularly before noon. The model shows the highest value in 08:00 LT, decreasing until the early afternoon, and then increasing again after 14:00 LT. The minimum model column value in the afternoon is approximately 40% lower than the maximum value at 08:00 LT (Supplementary Table 4). The observation that GEMS columns are lower than WRF-Chem columns in the early morning, but higher from noon to early afternoon, suggests that NO_x emissions are lower than the assumed constant emissions during nighttime and higher than the constant emissions during daytime.

In Fig. 2, GEMS shows broadly enhanced NO_2 columns over the Seoul-Gyeonggi region, peaking at its center, Seoul, where the column values reach approximately 20×10^{15}

184 molec (molecular) cm^{-2}. The plot clearly shows increased columns over a large area in Seoul
185 around 10:00–12:00 LT, a shrinkage of these plumes at 14:00 LT, and slight increases again at
186 16:00 LT (follow dark red to black colored areas).

187 The NO_2 columns from Pandora, a direct-sun spectrometer that retrieves the NO_2 with
188 a spectral resolution of 0.5 nm using wavelength ranges from 270 to 530 nm, show a significant
189 peak from mid to late morning at several locations across the Seoul-Gyeonggi region, similar
190 to the GEMS columns over Seoul[25]. Additionally, NO_2 columns measured from the Airborne
191 Compact Atmospheric Mapper (ACAM), which uses the ultraviolet and visible band from 304
192 to 520 nm with spectral resolution of 0.8 nm onboard the UC-12 aircraft, did not display an
193 early morning peak, which is consistent with the GEMS data[26]. Further validation[35] of the
194 GEMS L2 NO_2 product using 1 year of the tropospheric NO_2 columns IUP-UB (Institute of
195 Environmental Physics at the University of Bremen) product, TROPOMI product, and ground-
196 based measurements has demonstrated a correlation coefficient of 0.76, despite a general
197 overestimation in most regions. The diurnal variation captured by GEMS observation also
198 showed good agreement with ground-based observations, with variations depending on local
199 pollution levels. These findings further support the reliability of GEMS in monitoring NO_2
200 diurnal variations and emphasize the importance of regional emission characteristics in
201 interpreting early morning peaks.

202 In Fig. 3, the top-down emissions in Seoul, estimated from GEMS data under a steady-
203 state assumption (TD_S) using a simple mass balance approach, exhibit a peak at 12:00 LT.
204 However, the model results using TD_S did not reproduce the observed diurnal variations of
205 GEMS NO_2 columns (correlation coefficient = -0.23) (Fig. 3). Another top-down emission
206 estimation based on a non-steady-state assumption (TD_NS) reproduces the observed columns;
207 it shows high emissions during the early to mid-morning (peaking between 9:00 and 11:00 LT)
208 and reduced emissions from noon to the afternoon. The recent studies also addressed the need

209 for non-steady state approaches[36,37]. The model results using TD_NS closely replicated the
210 GEMS observations, which peaked between 10:00 and 12:00 LT, achieving the highest
211 correlation coefficient (0.88) and the lowest root-mean-square error (RMSE). Our study
212 highlights the importance of morning emission accumulation in driving maximum NO_2
213 columns between 10:00 and 12:00 LT in Seoul.

214 Top-down emission estimations in this study are explained in the Methods section and
215 Supplementary Figs. 8-12 and Supplementary Table 5. Details on the top-down emission
216 estimation method with non-steady state assumption will be discussed later for certain source
217 regions in South Asia.

218

219 - ***Beijing***

220 Similar to Seoul, GEMS NO_2 columns in Beijing exhibits a peak at 10:00 LT and trough
221 at 16:00 LT. The model diurnal pattern, assuming constant emissions, shows higher NO_2
222 columns than GEMS from 08:00 LT to 10:00 LT, and lower values from 10:00 LT to 14:00
223 LT. High nighttime emissions in the constant emission case cause large model columns in the
224 early morning (Fig. 3). The top-down NO_x emissions with a steady state assumption (TD_S)
225 in Beijing peak between 11:00 LT and 12:00 LT (Fig. 3). The top-down NOx emissions under
226 a non-steady-state assumption (TD_NS) in Beijing show a higher peak at 11:00 LT and lower
227 trough values in the late afternoon compared to those under a steady-state assumption (Fig. 3).
228 The model results using the control emissions and both TD_S and TD_NS show higher NO_2
229 column values than GEMS in the early morning but agree more closely with GEMS
230 observations in the mid-day. In the late afternoon, the model using TD_S and TD_NS shows
231 higher NO_2 columns again, but TD_NS compared to TD_S led to smaller biases. Among these,
232 the TD_NS results exhibit the highest correlation and the lowest RMSE value. The discrepancy
233 between the model and GEMS values in the early morning may stem from elevated nighttime

234 NO_x emissions used in this study. These findings highlight the importance of accurately
235 representing nighttime NO_x emissions and their associated chemistry to improve predictions of
236 NO_2 columns in the early morning. The ratio of NO_x to NO_2 is a parameter that is needed to
237 derive NO_x emissions from NO_2 observations. This parameter may add an uncertainty in
238 estimating top-down emissions in the morning. Beijing shows that emissions are higher in mid-
239 to-late morning than during early morning commuting hours in the top-down emissions with a
240 non-steady-state assumption. In this city, the minimum GEMS (model) column value in the
241 afternoon is approximately 30% (45%) lower than the maximum value in the late morning
242 (Supplementary Table 4).

243

244 - ***Yangtze River Delta (Shanghai and its surrounding areas)***

245 The Yangtze River Delta region in this study is a large area including Shanghai and
246 nearby cities (Fig. 2). In Fig. 1, GEMS NO_2 columns in this area peaks at 08:00 LT and reach
247 a minimum at 13:00 LT, with a relatively small difference between maximum and minimum
248 (the ratio of minimum to maximum is 0.83). The model column also shows a peak at 08:00 LT,
249 but decreases more rapidly over time compared to the GEMS data (Fig. 1). Interestingly, the
250 top-down NO_x emissions (both TD_S and TD_NS) over the Yangtze River Delta exhibit the
251 lowest value at 08:00 LT and increases until 16:00 LT (Fig. 3). Note that GEMS NO_2 columns
252 at 16:00 LT is high and comparable to those at 10:00 LT (Fig. 2). This may reflect unique
253 traffic patterns in the Yangtze River Delta cities or be related to port activities. Due to minimal
254 temporal variations in GEMS NO_2 columns over the Yangtze River Delta, the results of TD_S
255 and TD_NS are similar. The model results based on top-down emissions demonstrate the
256 highest correlation with observations and the lowest RMSE, underscoring the value of GEMS
257 data. The increase in NO_x emissions during the day may impact photochemistry relevant to

surface ozone and aerosols. Further study using in-situ observations and chemical transport models is needed to quantify the effects of diurnal variations of NO_x emission over the Yangtze River Delta.

- ***Guangzhou, Bangkok, and Hanoi***

In Guangzhou, Bangkok, and Hanoi, GEMS NO_2 columns are slightly higher than the model columns in the morning but slightly lower in the afternoon (Fig. 1). The spatial distribution of GEMS NO_2 columns highlights large GEMS NO_2 plumes over these cities, particularly in the early morning (Fig. 2). In contrast to Hanoi, Haiphong and Nam Dinh, located east and south of Hanoi respectively, show persistently high NO_2 columns throughout the day (Fig. 2 and Supplementary Figs. 6-7). This pattern may be attributed to traffic routes connecting Hanoi, Haiphong, and Nam Dinh. In Guangzhou and Bangkok, the minimum values in GEMS columns show approximately a 30% reduction from the maximum values. This reduction is even more significant in Hanoi, where it reaches 40% (Supplementary Table 4). Guangzhou, Bangkok, and Hanoi exhibit notably high top-down NO_x emissions early in the morning, followed by a rapid decrease toward noon under the non-steady-state assumption (TD_NS) (Fig. 3). Model results using TD_NS achieve the highest correlation ($R = 0.92–0.96$) and the lowest RMSE, whereas bottom-up emissions and top-down emissions under a steady-state assumption show poor correlations with GEMS observations.

Unexpectedly, the NO_x chemical lifetime (τ_c) in Hanoi, calculated based on chemical loss through HNO_3 formation via reaction with OH or N_2O_5 heterogeneous uptake, is the longest among all source regions (Supplementary Table 5). In Hanoi, the modeled OH concentration is the lowest among all source regions. Further analysis suggests that extremely high isoprene emissions in this region deplete OH[38,39], thereby potentially increasing the NO_x

chemical lifetime (Supplementary Figs. 10-11[40,41]). A comparison of WRF-Chem HCHO and TROPOMI HCHO columns reveals significant positive model biases south of 30°N in the domain, particularly in Hanoi, power plant regions in India, and countries near the Strait of Malacca. These biases are partly attributed to overestimated biogenic volatile organic compound emissions, including isoprene (Supplementary Fig. 11). This model deficiency affects the accuracy of top-down emission estimates. Consequently, in this study, we utilized τ_r, a surrogate for the directly calculated chemical lifetime (τ_c). τ_r is indirectly derived from a non-steady-state mass balance equation based on WRF-Chem results (Methods section). Under non-steady-state assumptions, τ_r yields non-negative top-down NO_x emissions in Hanoi, unlike τ_c.

- ***Chinese Power Plant Regions (Wuhai and Baotou)***

Besides cities, the GEMS NO_2 column was also analyzed for power plants and shipping routes. Fig. 2 and Supplementary Fig. 3 provide enhanced GEMS columns near power plants located in Wuhai and Baotou and their proximity in north China and northeastern India. Details about power plants in each location are provided in Supplementary Fig. 2 and Supplementary Table 3. Fig. 2 also illustrates NO_2 plumes from ship tracks detected by GEMS in the Strait of Malacca. In Wuhai and Baotou, similar to Seoul and Beijing, GEMS NO_2 columns peak in the late morning around 11:00 LT and decrease over time (Fig. 1). The minimum GEMS values are only 20% lower than the maximum values in Wuhai and Baotou, whereas the model using constant emission shows approximately a 40-50% decrease. The model columns are significantly higher than GEMS columns in the early morning and lower in the afternoon. Top-down NO_x emissions with a steady-state assumption (TD_S) peak at noon, but show small variations throughout the day in the regions around Chinese power plants (Fig. 3). Top-down

306 NO_x emissions under a non-steady-state assumption (TD_NS) exhibit a moderate peak in the
307 late morning over Wuhai and a sharp peak in the early morning over Baotou. In the studied
308 region, both power plants and other area source regions play significant roles, contributing to
309 the diurnal variations in GEMS NO_2 columns over power plants in China, which to some extent
310 resemble patterns observed in cities. The model results using both TD_S and TD_NS show
311 good correlation and low RMSE for Wuhai. For Baotou, the results using TD_NS exhibit the
312 highest correlation and the lowest RMSE.

313

314 - ***Indian Power Plant Regions***

315 In Indian power plant regions, the GEMS NO_2 columns typically peak around 08:30
316 LT, gradually decreasing thereafter (Fig. 1). These GEMS columns are slightly higher than the
317 model columns in the early morning but diminish in the afternoon. The GEMS minimum values
318 in the India P1, P2, and P3 regions experience significant reductions, with drops of 34%, 32%,
319 and 37%, respectively, from their maximum values. In contrast, the model exhibits smaller
320 reductions of 17%, 23%, and 25% for the India P1, P2, and P3 regions, respectively
321 (Supplementary Table 4). Top-down NO_x emissions with a steady-state assumption for these
322 power plants in India peak in the early morning and gradually decrease over time, as shown in
323 Supplementary Fig. 12. In contrast, top-down NO_x emission calculations based on a non-
324 steady-state assumption yield negative emissions for most power plant regions in India even
325 using τ_r. This is attributed to the significant negative temporal change terms and smaller
326 chemical sink terms, which result from longer chemical lifetimes and lower OH concentrations
327 compared to the power plant regions in China (Supplementary Table 5 and Supplementary
328 Figs. 10-12).

329

- ***Strait of Malacca (shipping source region)***

GEMS NO_2 along the ship routes in the Strait of Malacca reach their peak at 09:00 LT, declining over time (Fig. 1). The minimum GEMS value in the late afternoon is 40% lower than the maximum observed in the early morning. The model exhibits an even more substantial reduction, at 60%, in the Strait of Malacca (Supplementary Table 4). Interestingly, as shown in Supplementary Fig. 12, the derived top-down NO_x emissions with a steady-state assumption increase steadily throughout the day. Top-down NO_x emission calculations based on a non-steady-state assumption yield negative emissions for the Strait of Malacca, similar to those observed in power plant regions in India (Supplementary Table 5). Both model results using bottom-up and available top-down emission show strong correlations (correlation coefficient = ~1) with GEMS data (Supplementary Fig. 12).

Transport of NO_2 plumes

When atmospheric species are transported to a receptor area, the transported species can influence changes in both the temporal and spatial distribution of the species and their products in the receptor area[42,43]. GEMS have, for the first time, captured the hourly transport of NO_2 plumes from Seoul and several other hotspots in the Korean peninsula to receptor regions several hundred kilometers away (Fig. 4). In this study, in order to present the possibility of hourly scale observation for NO_2 transport, we could briefly touch on this long-range transport case study. Therefore, we just focused on two long-range transport events that occurred in the same period (March 22, 2021) which were determined by method adopted from the previous study[44]. The difference from this previous study is that we used a simple approach with the ECMWF Reanalysis v5 (ERA5) wind data[45] to compare with the movement of the NO_2 plume, rather than using the more precise and advanced hybrid single particle Lagrangian

integrated trajectory (HYSPLIT) model for event detection. Therefore, this brief case study can be extended with more profound interpretations in future studies. On March 22, 2021, a large NO_2 plume over Seoul and its surroundings at 09:45 LT (Fig. 4, red box; case (A)) was transported southeast until 14:45 LT, reaching Jecheon, Yeongju, and Uljin, where it was widespread. These three receptor cities had no substantial NO_x emission sources, and their NO_2 column values were low at 09:45 LT on March 22 but substantially higher between 11:45 and 14:45 LT (Supplementary Fig. 13). NO_x emissions in Jecheon, Yeongju, and Uljin are 12%, 6%, 1% of the emissions in Seoul, respectively. NO_2 was transported from hotspots including Gwangyang, Busan, and Pohang (southeastern coastline, Korean Peninsula; blue box; case (B), Fig. 4) to the Korea Strait between South Korea and Japan, with several distinct long NO_2 trails (Fig. 4, blue box; case (B)). The plume transport directions observed by GEMS were consistent with the wind directions (based on ECMWF ERA5 data) at 1,000 hPa (Supplementary Fig. 14). The winds are weak and varies in direction during the morning (10:00–12:00 LT) in the regions marked as red box. However, in the afternoon (13:00–15:00), the wind blows strongly toward the east. In addition, winds blow from the southern part of the Korean Peninsula toward Kagoshima, Japan at speeds greater than 5 m/s. In Fig. 4 (g and h), we included the spatial distributions of NO_2 at 13:45 and 14:45 to compare the long-range transport event on March 22 with March 23, when no long-range transport occurred.

The transported NO_2 contributed to the enhancement at the receptor areas, which led to substantial hourly changes in the NO_2 spatial distributions over the southern parts of the Korean Peninsula and its surroundings. The NO_x emissions estimated based on satellite measurements can be biased depending on the transported amount and transport frequency in the receptor areas. It is important to understand the temporal and spatial distribution of NO_2 in each area because it can help establish an appropriate NO_x control strategy by correcting the temporally biased NO_x levels available at a single time per day in each area.

Conclusions

The findings from the GEMS reported in the present study reveal that diurnal tropospheric NO_2 characteristics vary widely across various source regions. The top-down NO_x emissions obtained from tropospheric NO_2 column data derived from twice-a-day LEO measurements can be improved using GEO observations, such as GEMS. This improvement is possible because the emissions were calculated based on the assumption that both the chemistry and the diurnal variation of emissions are accurate, due to the absence of diurnally available NO_2 spatial distribution information. In addition, hourly tropospheric NO_2 column data, which can constrain both emissions and chemistry, can be utilized to assess diurnal NO_x emissions and improve the current NO_x emissions estimations from bottom-up emission inventory. In contrast to previous simple mass balance methods with a steady-state assumption, our study emphasizes the importance of including the temporal change in GEMS NO_2 columns, which reflects the carry-over of NO_2 over time in top-down emission estimations. Top-down emission estimations with non-steady-state assumption show an increase in NO_x emissions at a given time in the morning, followed by an increase in NO_2 column at later times. Conversely, a decrease in NO_x emissions at noon or in the early afternoon is followed by a decrease in NO_2 columns at later times. For example, in Seoul, our optimal top-down NO_x emission peaks between 9-11 LT, followed by NO_2 columns peaking between 10-12 LT. Meanwhile, the minimum NO_x emissions occur at 14 LT, followed by the minimum NO_2 columns at 15 LT. For most source regions, top-down NO_x emission estimations based on non-steady-state assumption utilizing hourly varying GEMS observations results in the most accurate NO_2 column simulations.

This study also highlights the challenges associated with this top-down approach. Accurate estimations of chemical lifetime, derived from relevant chemical reactions in the

chemical transport model, can be difficult, as observed in Hanoi, power plants in India, and the Strait of Malacca, where large biogenic emissions in the source region or nearby areas rapidly deplete OH and, thereby increasing the chemical lifetime of NO_x. In such cases, evaluating the biogenic emission estimates in the model becomes crucial. Additionally, uncertainties surrounding nighttime NO_x emissions and the chemistry influencing early morning NO_2 columns, which can vary by location, present another critical factor for improving model NO_2 simulations in the morning. In general, uncertainties in the chemical transport model, stemming from factors such as anthropogenic and biogenic emissions, chemical mechanisms, spatial resolution, and other physical processes, need further investigation.

The possibility of increasing uncertainties in GEMS tropospheric NO_2 column retrievals rise with increasing solar zenith angle, such as in the early morning or late afternoon. Therefore, a more thorough evaluation of GEMS data and model results using independent in-situ and remote sensing observations from surface and aircraft (e.g., Airborne and Satellite Investigation of Asian Air Quality, ASIA-AQ, https://www-air.larc.nasa.gov/missions/asia-aq/index.html) is necessary to accurately assess diurnal profiles in bottom-up emission inventories and to develop precise top-down NO_x emission estimates utilizing GEMS measurements. This study lays the groundwork and provides direction for future research efforts.

Methods

Geostationary Environmental Monitoring Spectrometer

GEMS build on the technology and algorithms of heritage instruments and augments various applications through unprecedented hourly observations. GEMS is the first UV–visible

426 hyperspectrometer in geostationary orbit and was launched aboard GEO-KOMPSAT-2B on
427 February 18, 2020. It provides daytime measurements of solar radiance reflected at the surface
428 and scattered in the atmosphere. Measurements are made in the 300–500 nm range, with a
429 mean spectral resolution of 0.6 nm in full width at half maximum (FWHM)[20]. The
430 backscattered solar radiance contains information on Rayleigh and Mie scattering, surface
431 albedo, and atmospheric trace gas absorption, including that of NO_2. These measurements
432 allow the observation of key air quality components, such as NO_2, sulfur dioxide (SO_2), ozone
433 (O_3), formaldehyde (HCHO), glyoxal (CHOCHO), and aerosols, at a spatial resolution of 3.5
434 × 7.7 km^2. GEMS is the first and only space-based instrument to provide daily time-resolved
435 (hourly) observations of these species. The field of regard of GEMS covers 20 countries in
436 Asia, extending E–W from Japan to India, and N–S from Mongolia to Indonesia
437 (Supplementary Fig. 1 and Supplementary Table 1)[20].

438

439 **Retrieval methods**

440 This study introduces new GEMS primary products: diurnal total and tropospheric NO_2
441 column variations retrieved in real-time over cities, industrial areas, and ports in Asia. In
442 addition, diurnal patterns are discussed. The NO_2 slant column density (SCD), i.e., the NO_2
443 concentration integrated along the light path through the atmosphere, was retrieved from the
444 GEMS radiance and irradiance spectra using the differential optical absorption spectroscopy
445 (DOAS)[46]. Spectral fitting was applied over the wavelength range of 432–450 nm, with the
446 absorption cross-sections convoluted using the GEMS instrument function (FWHM = 0.6 nm).
447 The absorption cross sections used were NO_2 (220 K[47]), O_3 (243 and 293 K[48]), O_4[49], H_2O[50],
448 and ring spectrum[51]. The SCD was converted to the NO_2 column by dividing it by the air mass
449 factor (AMF; VCD = SCD/AMF). Here, the AMF represents the ratio of the NO_2 column

integrated along the light path to the vertical NO_2 column for a selected spectral fitting window[20]. The AMF was calculated using the linearized pseudo-spherical scalar and vector discrete ordinate radiative transfer model[52], *a priori* NO_2 vertical profile shapes from the regional chemical transport model with the horizontal resolution of 28 x 28 km^2 (WRF-Chem[53] and the community atmosphere model with chemistry[54]), and ancillary data such as aerosol optical depth, aerosol effective height, surface reflectance, total ozone column, pressure, and geometries. Details of the GEMS NO_2 column density retrieval method has been published elsewhere[20].

The tropospheric NO_2 column density was calculated by subtracting the stratospheric NO_2 column density from the total NO_2 column density. The stratospheric NO_2 column density was estimated by scaling the stratospheric NO_2 column density from the single-layer isentropic model of chemistry and transport (SLIMCAT)[55,56] using GEMS NO_2 column densities observed over the Pacific Ocean, where negligible tropospheric NO_2 concentrations are expected. Over polluted areas, total NO_2 column diurnal variations appear to be dominated by tropospheric column variations. The mean value of the stratospheric NO_2 column over the GEMS domain, based on SLIMCAT estimation, was 0.1×10^{16} molec cm^{-2} (Supplementary Fig. 15).

Assessment of GEMS NO_2 data

GEMS vs. TROPOMI and OMI

GEMS total and tropospheric NO_2 column data were compared with TROPOMI and OMI data for observations at 04:45 coordinated UTC and 13:45 LT for June–August 2021 (Supplementary Table 6). TROPOMI, aboard the Sentinel-5P satellite, is the most recently

launched instrument capable of monitoring NO_2 column density from space with high temporospatial resolution (up to 5.5 × 3.5 km^2 pixels with daily revisit). Extensive validation of TROPOMI data has been published[56–58,61]. The correlation coefficients between the GEMS and TROPOMI (OMI) total NO_2 column densities were 0.78 (0.58), slopes were 1.87 (0.58), and intercepts were −0.36 (0.23) × 10^{16} molec cm^{-2}; for the GEMS and TROPOMI (OMI) tropospheric NO_2 column densities, the correlation coefficients were 0.63 (0.76), slopes were 1.27 (0.83), and intercepts were 0.06 (0.13) × 10^{16} molec cm^{-2} for the period June–August 2021 (Supplementary Table 6). These differences in statistics between the comparisons of GEMS and OMI, as well as GEMS and TROPOMI, can be influenced by the differences in spatial resolution of each satellite[62]. In addition, the differences in parameters between the total columns of GEMS and TROPOMI can be partly attributed to differences in the input data used to calculate their respective AMFs[20,57,59,60]. Differences between stratospheric and tropospheric partition algorithms are likely to contribute to differences in the tropospheric columns. GEMS tropospheric columns were obtained by subtracting SLIMCAT-based stratospheric NO_2 data from GEMS total columns, whereas those of TROPOMI were obtained using a data assimilation system[60] based on the TM5-MP model data[63]. Although both the total and tropospheric NO_2 column data observed from GEMS tended to be higher than those of TROPOMI, NO_2 column data agreed well[29,31,35] with those of TROPOMI, which have already been validated using ground-based MAX-DOAS and Pandora measurements[56,58,61].

GEMS vs. ground-based Pandora and MAX-DOAS

GEMS NO_2 data were compared with Pandora and MAX-DOAS data available for the two metropolitan cities of Seoul (South Korea), Xianghe (China), and a suburban area of Seosan (South Korea). The ground-based Pandora instrument, which uses direct sunlight as the

light source, produces NO_2 total column data[64,65]. Pandora measurements have been used to evaluate NO_2 column densities retrieved by TROPOMI and OMI[56,58,61,64–68]. GEMS total NO_2 column data were compared with the Pandonia Global Networks (PGN) NO_2 column data (https://pandonia-global-network.org/, last accessed March 16, 2024) in Seoul for the period June–August 2021. The correlation coefficient, slope, and intercept against Pandora are 0.78, 0.93, and 0.13×10^{16} molec cm^{-2}, respectively; (Supplementary Table 6). The GEMS total NO_2 column data were also compared with those of Pandora at Seosan, a suburban area of South Korea, for the first GEMS map of the air pollution campaign period from October 12 to November 27, 2020. The spectral fitting interval and absorption cross-sections adopted by PGN[69] were used to retrieve the NO_2 column data from the Pandora measurements during the campaign. The correlation coefficient, slope, and intercept were 0.74, 0.54, and 0.37×10^{16} molec cm^{-2}, respectively; (Supplementary Table 6). The GEMS NO_2 column densities tended to be lower than those of Pandora in both Seoul megacity and Seosan suburban areas. GEMS tropospheric NO_2 column data were also compared with those of the multi-axis differential optical absorption spectroscopy (MAX-DOAS) at Xianghe city[70] for the period June–August 2021. The correlation coefficient, slope, and intercept were 0.51, 0.13, and 1.42×10^{16} molec cm^{-2}, respectively, between GEMS tropospheric NO_2 columns and those of MAX-DOAS (Supplementary Table 6). This tendency of underestimation in GEMS NO_2 columns can be due to differences in vertical sensitivities in the lower atmosphere[71] and the relatively large GEMS footprint[72]. A similar underestimation tendency was also found in the comparisons of TROPOMI and OMI NO_2 data with those of Pandora and MAX-DOAS[56,58,61,64–74]. GEMS provides a representative value for an entire pixel, whereas MAX-DOAS measures NO_2 concentrations at a specific location. This fundamental difference in spatial resolution can lead to discrepancies in observed NO_2 variations, particularly in highly polluted areas. In such regions, localized emission sources and meteorological conditions can cause significant within

pixel variability, which MAX-DOAS captures but GEMS averages over a broader area. As a result, this differences in observation may contribute to differences in the timing and magnitude of NO_2 peaks observed by the two observations[56,71,72].

To understand vertical sensitivities of the GEMS retrieval over the course of the day, we investigated the discrepancy in either diurnal or measurement geometry variability between GEMS NO_2 and those measured by MAX-DOAS. Especially, MAX-DOAS is known to have a high sensitivity to surface NO_2[70,71]. Supplementary Figs. 16-18 show tropospheric NO_2 column measured from the GEMS and MAX-DOAS observation, SZA and VZA, and aerosol optical depth (AOD) and cloud fraction (CF) as a function of local time (LT). The diurnal variations captured in GEMS and MAX-DOAS are quite similar. Absolute difference between GEMS and MAX-DOAS tropospheric NO_2 columns tend to be large from 8:45 to 10:45 LT when the SZA is large (from 24.0 to 49.6°) and decreases at noon when the SZA is small (from 13.5 to 19.7°), and then increases again after 14:45 LT when the SZA becomes larger (from 32.5 to 46.1°). CF does not have a significant effect on the difference between tropospheric NO_2 from GEMS and MAX-DOAS, and AOD is higher in Seoul than in Kasuga, which leads to the overall difference between GEMS and MAX-DOAS being larger in Seoul than in Kasuga. These results mean that different geometry conditions and aerosols may affect the sensitivities to retrieve the surface gases under certain conditions.

Bottom-up emission inventory

The bottom-up anthropogenic emissions inventory for Asia used in this study is based on the Air Quality in Northeast Asia (AQNEA) emission inventory for Northeast Asia and the Comprehensive Regional Emissions inventory for Atmospheric Transport Experiment (CREATE) for the rest of Asian domain[75,76]. The AQNEA is a research project studying air

546 quality under various future carbon mitigation and air pollution control strategies using
547 multiple Integrated Assessment Models (IAMs) from participating regional and international
548 institutions. Emissions of six countries – China, South Korea, Japan, North Korea, Mongolia,
549 and Russia – in Northeast Asia were estimated in the AQNEA inventory. The inventory covers
550 eight criteria air pollutants - CO, SO_2, NO_x, non-methane volatile organic compounds
551 (NMVOCs), NH_3, PM_{10}, $PM_{2.5}$ - across eight emission sectors; power generation, industry,
552 residential, on-road/nonroad mobile, agriculture, solvent use, and waste. Annual emissions in
553 AQNEA for the year 2019 are as follows: 126.8 Tg for CO, 8.2 Tg for SO_2, 20.5 Tg for NO_x,
554 26.1 Tg NMVOCs, 10.6 Tg for NH_3, 11.6 Tg for PM_{10}, and 8.3 Tg. for $PM_{2.5}$. The inventory
555 was further processed using the SMOKE-Asia[75] emission processing model to generate spatio-
556 temporally allocated and chemically speciated emission fields in support of chemical transport
557 modeling. NO_x emissions in 2021 were reduced by 20% from AQNEA that represents the year
558 2019, following the trends in surface and satellite observations in Seoul, South Korea[77]. This
559 change does not represent whole region of interest.

560

561 **Top-down NO_x emission estimations with a steady-state assumption (TD_S)**

562 Top-down emissions of NO (E) can be estimated from NO_2 column (Ω) by dividing it
563 by an effective time scale τ_{eff}[78]. In this case, temporal change of column is ignored. The
564 observed column at a certain time is associated with the emission at the same time. The
565 effective time scale encapsulates the chemical loss of NO_2, and the conversion of NO_2 to NO,
566 depending on the special circumstances of the case. The advection effect is negligible
567 concerning a mass balance approach over a large source box. This effect may not be negligible
568 for small source regions or for spring, fall, and winter when NO_x lifetime is long[59].

$$E = \frac{\Omega}{\tau_{eff}} \qquad (1)$$

The effective time scale τ_{eff} can be derived from chemical transport models. In this study, we utilized the Weather Research Forecast-Chemistry (WRF-Chem) model results with various emission option to determine τ_{eff}. We use the same version and configuration of WRF-Chem as described in previous study and references therein[79] for July 2021. The bottom-up emission inventory combines data from AQNEA and CREATE. The model has horizontal resolution of 28 by 28 km^2 and 60 vertical layers up to 50 hPa. The Whole Atmosphere Community Climate Model (WACCM) forecast data is used for the chemical boundary/initial conditions.

$$\tau_{eff} = \frac{\Omega_{NO2\_WRFChem}}{E_{\mathrm{NO\_BU}}} \quad (2)$$

, where $\boldsymbol{\Omega_{NO2\_WRFChem}}$ is NO_2 columns calculated from WRF-Chem results and $E_{\mathrm{NO\_BU}}$ is bottom-up emission inventories used for the model runs. The top-down NO emission, $E_{\mathrm{NO\_TD}}$ is calculated from GEMS tropospheric NO_2 columns, $\boldsymbol{\Omega_{NO2\_GEMS}}$ and τ_{eff} from the chemical transport model.

589 $$E_{\mathrm{NO\_TD}} = \frac{\Omega_{NO2\_GEMS}}{\tau_{eff}} \quad (3)$$

590

591 In this study, we ran WRF-Chem from June 24 to July 31 using four different bottom-
592 up emission inventory values to account for uncertainties in the estimated effective lifetimes
593 and top-down NO emission (Table 1). Three emissions data used the same daily NO emissions
594 but adopt different diurnal variabilities, while one applied the minimum nighttime emission
595 value $E_{\mathrm{NO\_BU\_BG}}$ throughout the entire day to estimate background NO_2 column value
596 $\boldsymbol{\Omega_{NO2\_WRFChem\_BG}}$. In practice, in the total GEMS tropospheric NO_2 columns, the deviated part
597 from the background NO_2 columns is used to calculate the top-down NO emissions minimizing
598 the impacts of background value:

599

600 $$E_{\mathrm{NO\_TD}} = \frac{(\Omega_{NO2\_GEMS} - \Omega_{NO2\_WRFChem\_BG})}{\tau_{eff}} + E_{\mathrm{NO\_BU\_BG}}. \quad (4)$$

601

602 We estimated four different top-down NO emissions and primarily present the averaged
603 value. Details about four bottom-up and top-down emissions, corresponding WRF-Chem
604 simulations, and difference between top-down and bottom-up emissions are provided in
605 Supplementary Figs. 8, 9 and 12.

606

607 Table 1. Bottom-up emission inventories used for WRF-Chem simulations for development
608 of TD_S.

Bottom-Up (BU) Emission Inventory	Description

(WRF-Chem case name)	
BU1 (WRF-Chem1)	AQNEAV2 constant emissions using nighttime minimum value
BU2 (WRF-Chem2)	AQNEAV2 constant emissions (default value)
BU3 (WRF-Chem3)	AQNEAV2 with diurnal factor from EDGAR emission inventory
BU4 (WRF-Chem4)	AQNEAV2 with diurnal factor from Kim et al. (2016)

609

610 **Top-down NO_x emission estimations with non-steady-state assumption (TD_NS)**

611 The chemical lifetime of NO_2 (τ_c) against a reaction with OH during the daytime in
612 summer is relatively short, but generally exceeds one hour. As a result, the emissions at a given
613 time can influence NO_2 columns at later times, even in summer. The temporal change term
614 ($\partial\Omega/\partial t$) helps account for this memory effect when estimating NO_x emissions based on GEMS
615 hourly varying observations. With a non-steady-state assumption, emissions can be defined as:

616

617 $$E = \alpha\left(\frac{\partial\Omega}{\partial t} + \frac{\Omega}{\tau_c}\right) \qquad (5)$$

618

619 where $\boldsymbol{\alpha}$ is a conversion factor (NO_x/NO_2) that can be obtained from the model results. τ_c can
620 be directly calculated with reaction coefficients and reactant concentrations (e.g. [OH]).
621 Alternatively, this time scale can be derived from the model results as a residual of the equation,
622 using known bottom-up emission values, such as:

623

624 $$\tau_r = \frac{\Omega_{NO2\_WRFChem}}{\left(E_{\mathrm{NO\_BU}} - \frac{\partial\Omega_{NO2\_WRFChem}}{\partial t}\right)} \quad (6)$$

625

Here, τ_r is referred to as a residual time scale and is acquired from the WRF-Chem model results. With known τ_r values, the top-down emission is calculated with GEMS tropospheric NO_2 columns observations at a given time and the previous time, as follows:

$$E_{\mathrm{NO\_TD}} = \alpha \left(\frac{\partial \Omega_{NO_2 GEMS}}{\partial t} + \frac{\Omega_{NO_2 GEMS}}{\tau_r} \right) \qquad (7)$$

The temporal change term is calculated as an instantaneous gradient at the overpass time. In this way, we estimated another set of top-down NO_x emissions based on the non-steady state assumption using the equation above and WRF-Chem model results (TD_NS). In the Supplementary Table 5, τ_c and τ_r and OH concentrations averaged from 11 to 13 LT are summarized for each source. τ_c and τ_r are comparable for most sources, except for those with very low OH values such as Hanoi and the Strait of Malacca. For these two regions, τ_c is much larger than τ_r. In these cases, using τ_c instead of τ_r can result in negative top-down NO_x emissions. Therefore, in this study, we utilized τ_r values for estimating TD_NS. Even with τ_r values, the estimated top-down emissions can still be negative for power plants in India and the Strait of Malacca. As such, TD_NS for India P1, P2, and P3 and the Strait of Malacca are not presented in the main text in this manuscript. The results for these source regions are summarized in Supplementary Fig. 12.

Detection of long-range transport of NO_2 plumes

To determine the event case, we adopted a method from the previous study[44] that focused on the sulfur dioxide (SO_2) long-range transport detection and long-range transported SO_2 flowrate calculation using in-situ observation data, OMI satellite data, and the hybrid single particle Lagrangian integrated trajectory (HYSPLIT) model. However, in this study, we used satellite observation data and ECMWF Reanalysis v5 (ERA5) data[45] to detect the NO_2 long-range transportation event. First, we selected several cities (Jaecheon, Yeongju, and Uljin), located on the east side of Seoul, which have much lower NO_2 column densities than Seoul. The cities east of Seoul were considered for this study because the westerlies influenced the Korean Peninsula. Second, we identified the specific times when the NO_2 column densities increased by more than twice compared to the NO_2 column at the trough. This approach was used because the daily variability of NO_2 is not significant in the background region. Then, we found the dates when the peak of NO_2 columns was more than twice the trough of the day NO_2 column at Jaecheon, Yeongju, and Uljin. Lastly, we used ERA5 model wind field data to verify whether the movement of NO_2 plumes observed in GEMS data aligned with the wind direction in ERA5, and we selected the one event that was shown clearly visible in the satellite images as a case study of this study. In this study, we employed a simpler detection method to suggest the possibility of long-range transport. Therefore, a more precise approach would involve using backward trajectory models such as the FLEXible PARTicle dispersion (FLEXPART) model or HYSPLIT for long-range transport detection. Thus, a more detailed study is needed in the future.

667 # References

668 1. Menut, L., et al. Impact of realistic hourly emissions profiles on air pollutants
669 concentrations modelled with CHIMERE. *Atmos. Environ.* **49**, 233–244 (2012). doi:
670 10.1016/j.atmosenv.2011.11.057.

671 2. Stevenson, D. S., et al. Multimodel ensemble simulations of present-day and near-
672 future tropospheric ozone. *J. Geophys. Res. Atmos.* **111**, D08301 (2006). doi:
673 10.1029/2005JD006338.

674 3. Goldberg, D. L., et al. A top-down assessment using OMI NO_2 suggests an
675 underestimate in the NOx emissions inventory in Seoul, South Korea, during KORUS-AQ.
676 *Atmos. Chem. Phys.* **19**(3), 1801–1818 (2019). doi: 10.5194/acp-19-1801-2019.

677 4. Qu, Z., et al. Impacts of global NO_x inversions on NO_2 and ozone simulations. *Atmos.*
678 *Chem. Phys.* **20**(21), 13109–13130 (2020). doi: 10.5194/acp-20-13109-2020.

679 5. Fioletov, V., et al. Quantifying urban, industrial, and background changes in NO_2
680 during the COVID-19 lockdown period based on TROPOMI satellite observations. *Atmos.*
681 *Chem. Phys.* **22**(6), 4201–4236 (2022). doi: 10.5194/acp-22-4201-2022.

682 6. Sicard, P., et al. Trends in urban air pollution over the last two decades: A global
683 perspective. *Sci. Total Environ.* **858**, 160064 (2023). doi: 10.1016/j.scitotenv.2022.160064.

684 7. Georgoulias, A. K., et al. Trends and trend reversal detection in 2 decades of
685 tropospheric NO_2 satellite observations. *Atmos. Chem. Phys.* **19**(9), 6269–6294 (2019). doi:
686 10.5194/acp-19-6269-2019.

687 8. Krotkov, N. A., et al. Aura OMI observations of regional SO_2 and NO_2 pollution
688 changes from 2005 to 2015. *Atmos. Chem. Phys.* **16**(7), 4605–4629 (2016). doi: 10.5194/acp-
689 16-4605-2016.

690 9. Cooper, M. J., et al. Global fine-scale changes in ambient NO_2 during COVID-19
691 lockdowns. *Nature* **601**(7893), 380–387 (2022). doi: 10.1038/s41586-021-04229-0.

692 10. Boersma, K. F., et al. Improving algorithms and uncertainty estimates for satellite NO_2
693 retrievals: results from the quality assurance for the essential climate variables (QA4ECV)
694 project. *Atmos. Meas. Tech.* **11**(12), 6651–6678 (2018). doi: 10.5194/amt-11-6651-2018.
695 11. Lamsal, L. N., et al. Ozone Monitoring Instrument (OMI) Aura nitrogen dioxide
696 standard product version 4.0 with improved surface and cloud treatments. *Atmos. Meas.*
697 *Tech.* **14**(1), 455–479 (2021). doi: 10.5194/amt-14-455-2021.
698 12. Burrows, J. P., et al. The global ozone monitoring experiment (GOME): Mission
699 concept and first scientific results. *J. Atmos. Sci.* **56**(2), 151–175 (1999). doi: 10.1175/1520-
700 0469(1999)056<0151:TGOMEG>2.0.CO;2.
701 13. Callies, J., et al. GOME-2-Metop's second-generation sensor for operational ozone
702 monitoring. *ESA bull.* **102**, 28–36 (2000).
703 14. Bovensmann, H., et al. SCIAMACHY: Mission objectives and measurement modes. *J.*
704 *Atmos. Sci.* **56**(2), 127–150, (1999). doi: 10.1175/1520-
705 0469(1999)056<0127:SMOAMM>2.0.CO;2.
706 15. Levelt, P. F., et al. The ozone monitoring instrument. *IEEE Trans. Geosci. Remote Sens.*
707 **44**(5), 1093–1101 (2006). doi: 10.1109/TGRS.2006.872333.
708 16. Levelt, P. F., et al. The Ozone Monitoring Instrument: overview of 14 years in
709 space. *Atmos. Chem. Phys.* **18**(8), 5699–5745 (2018). doi: 10.5194/acp-18-5699-2018.
710 17. Veefkind, J. P., et al. TROPOMI on the ESA Sentinel-5 Precursor: A GMES mission
711 for global observations of the atmospheric composition for climate, air quality and ozone layer
712 applications. *Remote Sens. Environ.* **120**, 70–83 (2012). doi: 10.1016/j.rse.2011.09.027.
713 18. Richter, A., et al. Increase in tropospheric nitrogen dioxide over China observed from
714 space. *Nature* **437**(7055), 129–132 (2005). doi: 10.1038/nature04092.
715 19. A geostationary satellite constellation for observing global air quality: An international
716 path forward. CEOS Atmospheric Composition Constellation, Version 4, 41.

https://ceos.org/observations/documents/AC-VC_Geostationary-Cx-for-Global-AQ-final_Apr2011.pdf (2011).

20. Kim, J., et al. New era of air quality monitoring from space: Geostationary Environment Monitoring Spectrometer (GEMS). *Bull. Am. Meteorol. Soc.* **101**(1), E1–E22 (2020). doi: 10.1175/BAMS-D-18-0013.1.

21. Zoogman, P., et al. Tropospheric emissions: Monitoring of pollution (TEMPO). *J. Quant. Spectrosc. Radiat. Transf.* **186**, 17–39 (2017). doi: 10.1016/j.jqsrt.2016.05.008.

22. Fishman, J., et al. The United States' next generation of atmospheric composition and coastal ecosystem measurements: NASA's GEO stationary Coastal and Air Pollution Events (GEO-CAPE) mission. *Bull. Am. Meteorol. Soc.* **93**, 1547–1566 (2012). doi: 10.1175/BAMS-D-11-00201.1.

23. Lin, J-T., et al. Constraint of anthropogenic NOx emissions in China from different sectors: a new methodology using multiple satellite retrievals *Atmos. Chem. Phys.,* **10**, 63–78 (2010), doi: 10.5194/acp-10-63-2010.

24. Knepp, T., et al. Estimating surface NO_2 and SO_2 mixing ratios from fast-response total column observations and potential application to geostationary missions, *J. Atmos. Chem.*, **72**, 261–286, (2015), doi: 10.1007/s10874-013-9257-6.

25. Judd, L. M., et al. The Dawn of Geostationary Air Quality Monitoring: Case Studies From Seoul and Los Angeles, *Front. Environ. Sci.*, **6**, (2018), doi: 10.3389/fenvs.2018.00085.

26. Li, J., et al., Comprehensive evaluations of diurnal NO2 measurements during DISCOVER-AQ 2011: Effects of resolution-dependent representation of NOx emissions, *Atmos. Chem. Phys.*, **21**, 11133-11160, (2021), doi: 10.5194/acp-21-11133-2021.

27. Boersma, K. F., et al. Intercomparison of SCIAMACHY and OMI tropospheric NO_2 columns: Observing the diurnal evolution of chemistry and emissions from space. *J. Geophys. Res. Atmos.* **113**(D16) (2008). doi: 10.1029/2007JD008816.

28. Boersma, K. F., et al. Validation of urban NO_2 concentrations and their diurnal and seasonal variations observed from the SCIAMACHY and OMI sensors using in situ surface measurements in Israeli cities, *Atmos. Chem. Phys.*, **9**, 3867–3879, (2009), doi: 10.5194/acp-9-3867-2009.

29. Edwards, D. P., et al. Quantifying the diurnal variation in atmospheric NO_2 from Geostationary Environment Monitoring Spectrometer (GEMS) observations. *Atmos. Chem. Phys.* **24**(15), 8943–8961 (2024). doi: 10.5194/acp-24-8943-2024.

30. Yang, L. H., et al. Interpreting Geostationary Environment Monitoring Spectrometer (GEMS) geostationary satellite observations of the diurnal variation in nitrogen dioxide (NO_2) over East Asia. *Atmos. Chem. Phys.* **24**(12), 7027–7039 (2024). doi: 10.5194/acp-24-7027-2024.

31. Oak, Y. J., et al. A bias-corrected GEMS geostationary satellite product for nitrogen dioxide using machine learning to enforce consistency with the TROPOMI satellite instrument. *Atmos. Meas. Tech.* **17**(17), 5147–5159 (2024). doi: 10.5194/amt-17-5147-2024.

32. Ahmad, N., et al. Estimation of ground-level NO_2 and its spatiotemporal variations in China using GEMS measurements and a nested machine learning model. *Atmos. Chem. Phys.* **24**(16), 9645–9665 (2024). doi: 10.5194/acp-24-9645-2024.

33. He, Q., et al. Quantifying uncertainty in ML-derived atmosphere remote sensing: Hourly surface NO_2 estimation with GEMS. *Geophys. Res. Lett.* **51**(18), e2024GL110468 (2024). doi: 10.1029/2024GL110468.

34. Stavrakou, T., et al. Satellite evidence for changes in the NO_2 weekly cycle over large cities. *Sci Rep* **10**, 10066 (2020). doi: 10.1038/s41598-020-66891-0.

764 35. Lange, K., et al. Validation of GEMS tropospheric NO2 columns and their diurnal
765 variation with ground-based DOAS measurements. *Atmos. Meas. Tech.* **17**(21), 6315-6344
766 (2024). doi: 10.5194/amt-17-6315-2024.

767 36. Koene, E. F. M., et al. On the theory of the divergence method for quantifying source
768 emissions from satellite observations. *J. Geophys. Res. Atmos.* **129**(12), e2023JD039904
769 (2024). doi: 10.1029/2023JD039904.

770 37. Cifuentes, F., et al. Accurate space-based NOx emission estimates with the flux
771 divergence approach require fine-scale model information on local oxidation chemistry and
772 profile shapes. *Geosci. Model Dev.* **18**(3), 621-649 (2025). doi: 10.5194/gmd-18-621-2025.

773 38. Lelieveld, J., et al. On the role of hydroxyl radicals in the self-cleansing capacity of the
774 troposphere. *Atmos. Chem, Phys.* **4**(9/10), 2337-2344 (2004). doi: 10.5194/acp-4-2337-2004.

775 39. Kim, S. W., et al. Impact of turbulent mixing on isoprene chemistry. *Geophys. Res. Lett.*
776 **43**(14), 7701-7708 (2016). doi: 10.1002/2016GL069752.

777 40. De Smedt, I., et al. CCI+P HCHO tropospheric column L3 data from TROPOMI, v1
778 (Version 1) [Data set], Royal Belgian Institute for Space Aeronomy (2024).
779 https://doi.org/10.18758/2IMQEZ32.

780 41. Copernicus Sentinel-5P (processed by ESA), 2018, TROPOMI Level 2 Formaldehyde
781 Total Column products. Version 01. European Space Agency (2018).
782 https://doi.org/10.5270/S5P-tjlxfd2.

783 42. Qu, Y., et al. An overview of emissions of SO2 and NOx and the long-range transport
784 of oxidized sulfur and nitrogen pollutants in East Asia. *J. Environ. Sci.* **44**, 13-25 (2016). doi:
785 10.1016/j.jes.2015.08.028.

786 43. Jeong, U., et al. Assessing the effect of long-range pollutant transportation on air quality
787 in Seoul using the conditional potential source contribution function method. *Atmos. Environ.*
788 **150**, 33-44 (2017). doi: 10.1016/j.atmosenv.2016.11.017.

789 44. Park, J., et al. Long-range transport of SO_2 from continental Asia to northeast Asia and
790 the northwest Pacific ocean: flow rate estimation using OMI data, surface in situ data, and the
791 HYSPLIT model. *Atmosphere*, **7**(4), 53 (2016). doi: 10.3390/atmos7040053.

792 45. Hersbach. H., et al. ERA5 hourly data on single levels from 1940 to present, Copernicus
793 Climate Change Service (C3S) Climate Data Store, 2023. doi: 10.24381/cds.adbb2d47.

794 46. Platt, U. & Stutz, J. *Differential Optical Absorption Spectroscopy: Principles and*
795 *Applications*, Springer, Berlin, Heidelberg, 135–174 (2008).

796 47. Vandaele, A. C., et al. High-resolution Fourier transform measurement of the NO_2
797 visible and near-infrared absorption cross sections: Temperature and pressure effects. *J.*
798 *Geophys. Res.* **107**(D18), ACH-3 (2002). doi: 10.1029/2001JD000971.

799 48. Bogumil, K., et al. Measurements of molecular absorption spectra with the
800 SCIAMACHY pre-flight model: instrument characterization and reference data for
801 atmospheric remote-sensing in the 230–2380 nm region. *J. Photochem. Photobiol., A.* **157**(2–
802 3), 167–184 (2003). doi: 10.1016/S1010-6030(03)00062-5.

803 49. Thalman, R. & Volkamer, R. Temperature dependent absorption cross-sections of O_2–
804 O_2 collision pairs between 340 and 630 nm and at atmospherically relevant pressure. *Phys.*
805 *Chem. Chem. Phys.* **15**(37), 15371–15381 (2013). doi: 10.1039/C3CP50968K.

806 50. Rothman, L. S., et al. The HITRAN 2008 molecular spectroscopic database. *J. Quant.*
807 *Spectrosc. Radiat. Transf.* **110**(9–10), 533–572 (2009). doi: 10.1016/j.jqsrt.2009.02.013.

808 51. Chance, K. V. & Spurr, R. J. D. Ring effect studies: Rayleigh scattering, including

809 molecular parameters for rotational Raman scattering, and the Fraunhofer spectrum. *Appl.*
810 *Opt.* **36**(21), 5224–5230 (1997). doi: 10.1364/AO.36.005224.

811 52. Spurr, R. & Christi, M. On the generation of atmospheric property Jacobians from the
812 (V) LIDORT linearized radiative transfer models. *J. Quant. Spectrosc. Radiat. Transf.* **142**,
813 109–115 (2014). doi: 10.1016/j.jqsrt.2014.03.011.

814 53. Grell, G. A., et al. Fully coupled "online" chemistry within the WRF model. *Atmos.*
815 *Environ.* **39**(37), 6957–6975 (2005). doi: 10.1016/j.atmosenv.2005.04.027.

816 54. Emmons, L. K., et al. The chemistry mechanism in the community Earth system model
817 version2 (CESM2). *J. Adv. Model. Earth Syst.* **12**(4), e2019MS001882 (2020). doi:
818 10.1029/2019MS001882.

819 55. Chipperfield, M. P. New version of the TOMCAT/SLIMCAT off-line chemical
820 transport model: Intercomparison of stratospheric tracer experiments. *Q. J. R. Meteorol.*
821 *Soc.,* **132**(617), 1179–1203 (2006). doi: 10.1256/qj.05.51.

822 56. Verhoelst, T., et al. Ground-based validation of the Copernicus Sentinel-5p TROPOMI
823 NO_2 measurements with the NDACC ZSL-DOAS, MAX-DOAS and Pandonia global
824 networks. *Atmos. Meas. Tech*, **14**(1), 481–510 (2021). doi: 10.5194/amt-14-481-2021.

825 57. Van Geffen, J., et al. S5P TROPOMI NO_2 slant column retrieval: Method, stability,
826 uncertainties and comparisons with OMI. *Atmos. Meas. Tech.* **13**(3), 1315–1335 (2020). doi:
827 10.5194/amt-13-1315-2020.

828 58. Ialongo, I., et al. Comparison of TROPOMI/Sentinel-5 Precursor NO_2 observations
829 with ground-based measurements in Helsinki. *Atmos. Meas. Tech.* **13**(1), 205–218. (2020). doi:
830 10.5194/amt-13-205-2020.

831 59. Seo, S., et al. Diurnal variations of NO2 tropospheric vertical column density over the
832 Seoul metropolitan area from the Geostationary Environment Monitoring Spectrometer

(GEMS): seasonal differences and the influence of the a priori NO2 profile. *Atmos. Meas. Tech.* **18**(1), 115-128 (2025). doi: 10.5194/amt-18-115-2025.

60. van Geffen, J. H. G. M., et al. TROPOMI ATBD of the total and tropospheric NO_2 data products, Tech. Rep. S5P-KNMI-L2-0005-RP, Koninklijk Nederlands Meteorologisch Instituut (KNMI), CI-7430-ATBD, issue 1.4.0 (2019). https://sentinel.esa.int/documents/247904/2476257/sentinel-5p-tropomi-atbd-no2-data-products

61. Lambert, J., et al. *Quarterly Validation Report of the Copernicus Sentinel-5 Precursor Operational Data Products#* 06: April 2018–February 2020. Belgian Institute for Space Aeronomy: Uccle, Belgium (2020).

62. Judd, L. M., et al. Evaluating the impact of spatial resolution on tropospheric NO2 column comparisons within urban areas using high-resolution airborne data. *Atmos. Meas. Tech.* **12**(11), 6091-6111 (2019). doi: 10.5194/amt-12-6091-2019.

63. Williams, J. E., et al. The high-resolution version of TM5-MP for optimized satellite retrievals: description and validation. *Geosci. Model Dev.* **10**, 721–750 (2017). doi: 10.5194/gmd-10-721-2017.

64. Herman, J., et al. NO_2 column amounts from ground-based Pandora and MFDOAS spectrometers using the direct-Sun DOAS technique: Intercomparisons and application to OMI validation. *J. Geophys. Res. Atmos.* **114**(D13) (2009). doi: 10.1029/2009JD011848.

65. Herman, J., et al. Underestimation of column NO_2 amounts from the OMI satellite compared to diurnally varying ground-based retrievals from multiple PANDORA spectrometer instruments. *Atmos. Meas. Tech.* **12**(10), 5593–5612 (2019). doi: 10.5194/amt-12-5593-2019.

66. Zhao, X., et al. Assessment of the quality of TROPOMI high-spatial-resolution NO_2 data products in the Greater Toronto Area. *Atmos. Meas. Tech.* **13**(4), 2131–2159 (2020). doi: 10.5194/amt-13-2131-2020.

858 67. Judd, L. M., et al. Evaluating Sentinel-5P TROPOMI tropospheric NO_2 column
859 densities with airborne and Pandora spectrometers near New York City and Long Island
860 Sound. *Atmos. Meas. Tech.* **13**(11), 6113–6140 (2020). doi: 10.5194/amt-13-6113-2020.
861 68. Reed, A. J., et al. Effects of local meteorology and aerosols on ozone and nitrogen
862 dioxide retrievals from OMI and pandora spectrometers in Maryland, USA during
863 DISCOVER-AQ 2011. *J. Atmos. Chem.* **72**(3), 455–482 (2015). doi: 10.1007/s10874-013-
864 9254-9.
865 69. Cede, A., et al. (2019). TN on PGN products "correct use" guidelines, Pandonia Global
866 Network, available at: https://www.pandonia-global-network.org/wp-
867 content/uploads/2020/01/LuftBlick_FRM4AQ_PGNUserGuidelines_RP_2019009_v1.pdf (la
868 st access: 22 April 2022).
869 70. Hendrick, F., et al. Four years of ground-based MAX-DOAS observations of HONO
870 and NO_2 in the Beijing area. *Atmos. Chem. Phys.* **14**(2), 765–781 (2014). doi: 10.5194/acp-14-
871 765-2014.
872 71. Wagner, T., et al. Inversion of tropospheric profiles of aerosol extinction and HCHO
873 and NO_2 mixing ratios from MAX-DOAS observations in Milano during the summer of 2003
874 and comparison with independent data sets. *Atmos. Meas. Tech.* **4**(12), 2685-2715 (2011). doi:
875 10.5194/amt-4-2685-2011.
876 72. Chan, K. L., et al. MAX-DOAS measurements of tropospheric NO_2 and HCHO in
877 Munich and the comparison to OMI and TROPOMI satellite observations. *Atmos. Meas. Tech.*
878 **13**(8), 4499-4520 (2020). doi: 10.5194/amt-13-4499-2020.
879 73. Wang, C., et al. Comparison and Validation of TROPOMI and OMI NO_2 Observations
880 over China. *Atmosphere.* **11**(6), 636 (2020). doi: 10.3390/atmos11060636.
881 74. Park, J. U., et al. Spatiotemporal inhomogeneity of total column NO_2 in a polluted urban
882 area inferred from TROPOMI and Pandora intercomparisons. *GIScience & Remote Sens.* **59**(1),

883 354–373 (2022). doi: 10.1080/15481603.2022.2026640.
884 75. Woo, J.-H., et al. Development of an anthropogenic emissions processing system for
885 Asia using SMOKE. *Atmos. Environ.* 58, 5-13 (2012). doi: 10.1016/j.atmosenv.2011.10.042.
886 76. Woo, J.-H., et al. Development of a global integrated assessment model for climate-
887 air quality management focused on Northeast Asia (GUIDE-Global): A Framework Design.
888 https://pure.iiasa.ac.at/id/eprint/19501/ (2023).
889 77. Seo, S., et al. Reductions in NO_2 concentrations in Seoul, South Korea detected from
890 space and ground-based monitors prior to and during the COVID-19 pandemic. *Environ. Res.*
891 *Commun.* **3**, 051005 (2021). doi: 10.1088/2515-7620/abed92.
892 78. Martin, R. V., et al. Global inventory of nitrogen oxide emissions constrained by
893 space-based observations of NO_2 columns. *J. Geophys. Res. Atmos.* **108** (2003). doi:
894 10.1029/2003JD003453.
895 79. Kim, K.-M., et al. Sensitivity of the WRF-Chem v4. 4 simulations of ozone and
896 formaldehyde and their precursors to multiple bottom-up emission inventories over East Asia
897 during the KORUS-AQ 2016 field campaign. *Geosci. Model Dev.* **17**, 1931-1955 (2024). doi:
898 10.5194/gmd-17-1931-2024.

899

900

901

Acknowledgements

This research was supported by a grant from the National Institute of Environmental Research (NIER), funded by the Korea Ministry of Environment (MOE) of the Republic of Korea (NIER-2024-04-02-028). This work was supported by the National Research Foundation of Korea (NRF) grant funded by the Korea government (MSIT) (No. 2020R1A2C2014131). This work was supported by Korea Environmental Industry & Technology Institute (KEITI) through Climate Change R&D Project for New Climate Regime., funded by Korea Ministry of Environment (MOE)(RS-2022-KE002096). The MAX-DOAS and PGN instrument PIs and staff at the stations are grateful for their sustained effort in maintaining high-quality measurements and for valuable scientific discussions. The PGN is a bilateral project supported by funding from NASA and ESA.

Author information

Authors and Affiliations

Division of Earth Environmental System Science, Major of Spatial Information Engineering, Pukyong National University, Busan, Republic of Korea
Junsung Park, Hanlim Lee, Daewon Kim & Wonei Choi

Center for Astrophysics | Harvard & Smithsonian, Cambridge, Massachusetts, USA
Junsung Park

National Institute of Environmental Research, Incheon, Republic of Korea
Hyunkee Hong, Won-Jin Lee & Dong-Won Lee

Department of Atmospheric Sciences, Yonsei University, Seoul, Republic of Korea
Si-Wan Kim, Jhoon Kim, Seunghwan Seo & Kyoung-Min Kim

Irreversible Climate Change Research Center, Yonsei University, Seoul, Republic of Korea
Si-Wan Kim

Belgian Institute for Space Aeronomy (BIRA-IASB), Brussels, Belgium
Michel Van Roozendael & Caroline Fayt

Department of Climate and Energy Systems Engineering/Social Economy, Ewha Womans University, Seoul, Republic of Korea
Myong-Hwan Ahn

Harvard School of Engineering and Applied Science, Harvard University, Cambridge, Massachusetts, USA
Daniel J. Jacob

Institute of Environmental Studies, Pusan National University, Busan, Republic of Korea
Daewon Kim

NASA postdoctoral Program (NPP) at Goddard Space Flight Center, Greenbelt, Maryland, USA

Wonei Choi

Max-Planck Institute for Chemistry (MPI-C), Mainz, Germany
Thomas Wagner

Institute of Environmental Physics (IUP-UB), University of Bremen, Bremen, Germany
Andreas Richter

Atmospheric Chemistry and Dynamics Laboratory, NASA Goddard Space Flight Center, Greenbelt, Maryland, USA
Nickolay A. Krotkov & Lok N. Lamsal

University of Maryland Baltimore County (UMBC), Baltimore, Maryland, USA
Lok N. Lamsal

Bureau of Ocean Energy Management, Stirling, Virginia, USA
Lok N. Lamsal

Korea Aerospace Research Institute, Daejeon, Republic of Korea
Dai Ho Ko & Seung Hoon Lee

Department of Environmental Planning & Advanced Program for Urban Environmental Studies, Seoul National University
Jung-Hun Woo

Contributions

J.P., H.H., H.L., and S.W.K. designed the study. J.P., H.H., H.L., S.W.K., J.K., M.V.R., D.J.J., T.W., A.R., N.A.K., and L.N.L. contributed to writing the original manuscript. M.V.R. and C.F. supported the retrieval of NO_2 slant column density by providing the QDOAS software. M.H.A. contributed to the L1 dataset used for NO_2 slant column density retrieval. D.J.J., S.W.K., S.S., and K.M.K. contributed to the interpretation of chemistry and model simulations. D.K. and W.C. contributed to satellite analysis. Funding for the project was provided by H.H., W.J.L., D.W.L., and D.H.K. S.H.L. contributed to the development of the GEMS instrument. J.H.W. provided the emission inventory data. All authors contributed to the review, editing, and improvement of the manuscript.

Figure captions/legends

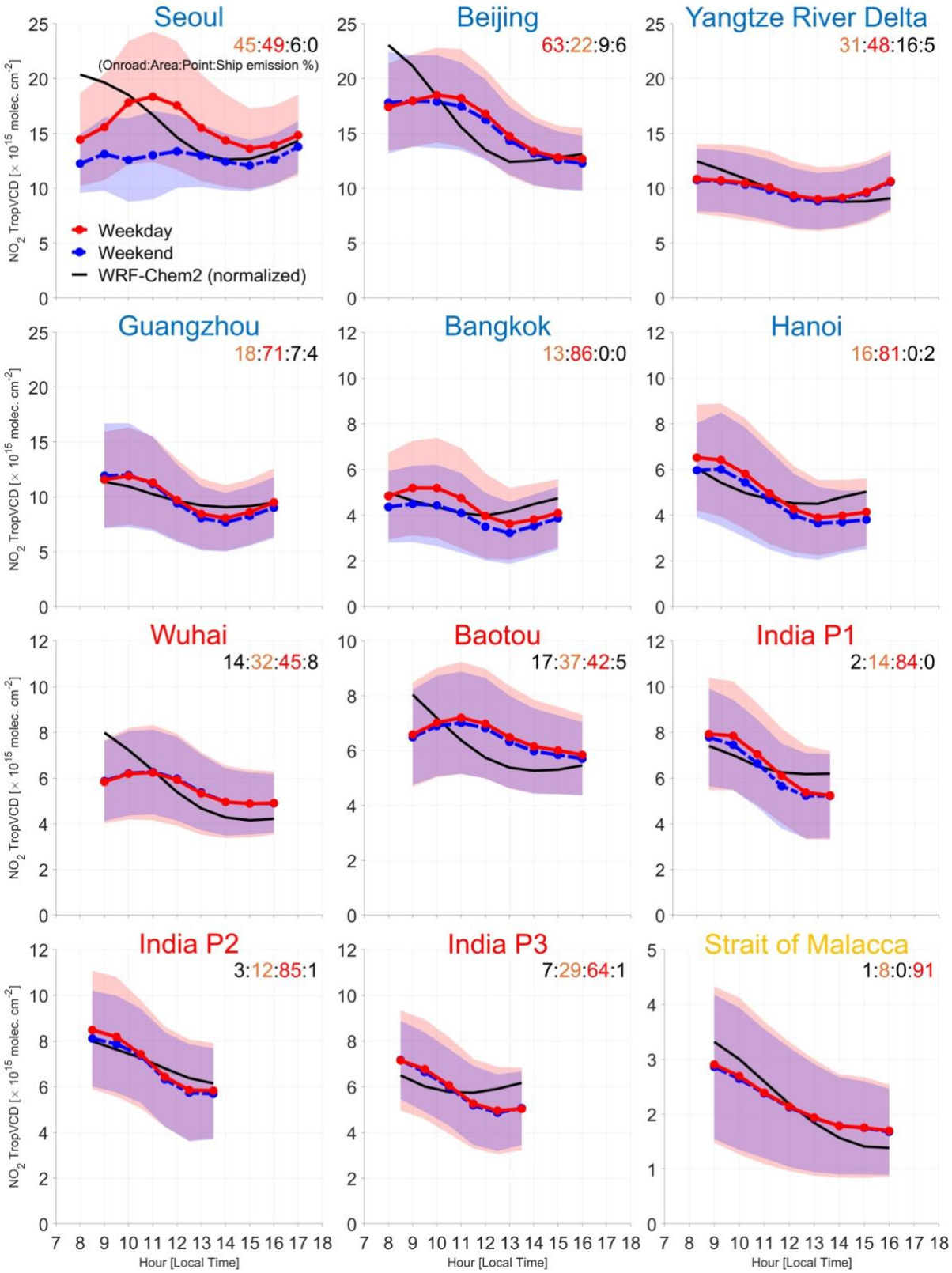

Fig. 1. Hourly variations in GEMS tropospheric NO_2 columns over major source regions during the study period (June, July, August 2021 and 2022). One standard deviation is

shaded. Red (blue) lines show weekday (weekend) values. Black line is NO_2 columns from WRF-Chem using a constant emission over time that are normalized to have the same daytime mean value as GEMS. Blue, red, and yellow labeled regions denote urban, power plant, and ship track sources, respectively. The source attribution from the bottom-up emission inventory is shown in top right corner. Contributions from on road, area, point, and ship emissions to the total NO_x emission (%) as in bottom-up emission inventory are provided. The largest and the second largest sectors are noted in red and orange, respectively. Here, area source represents mainly nonroad (offroad) and residential sources.

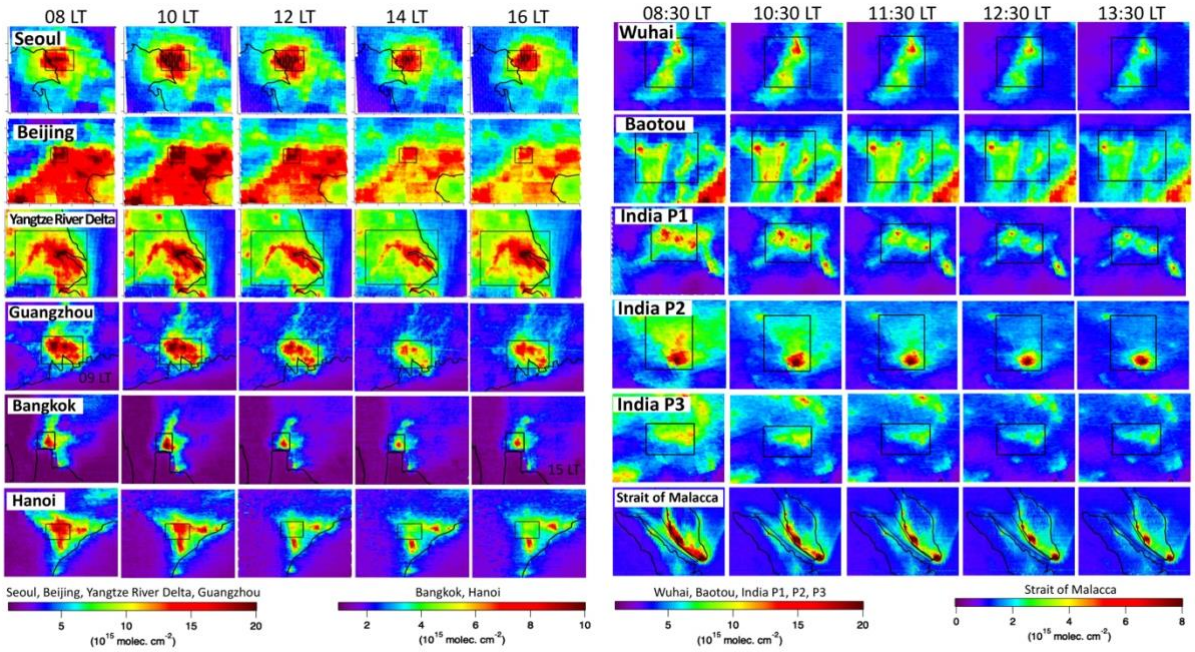

981

982 **Fig. 2. Hourly spatial distribution of average GEMS tropospheric NO_2 columns over**
983 **major source regions.** The observation times are indicated on the top of the plots. Different
984 times are noted in black on the map of Guangzhou (09 LT instead of 08 LT) and Bangkok (15
985 LT instead of 16 LT) according to the GEMS observation schedule. The latitude and longitude
986 information for each map is provided in Supplementary Data. Approximate local times are
987 shown for each source. The source boxes used for averaging data are exhibited with black
988 rectangles.

989

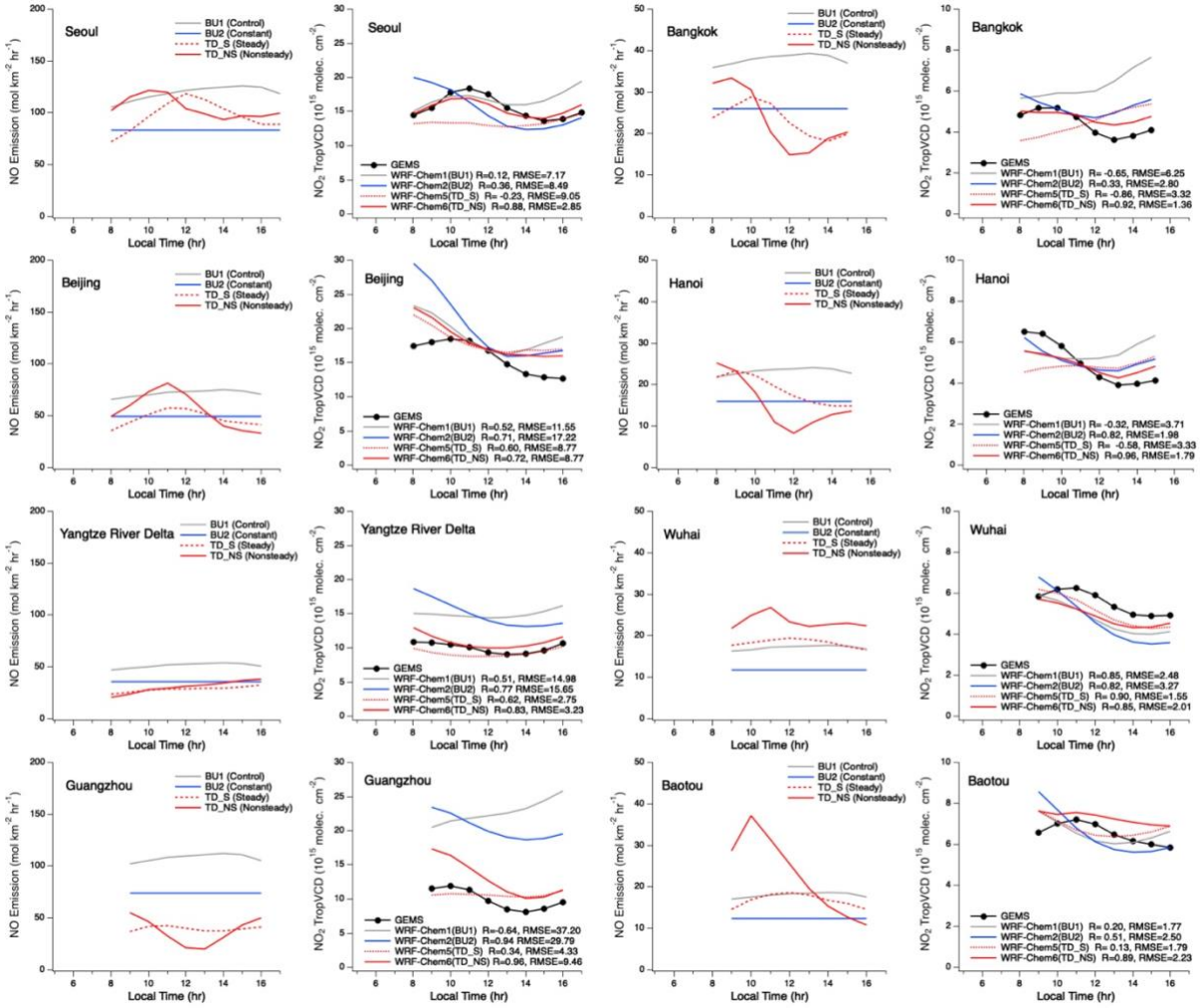

Fig. 3. Hourly variations in bottom-up and top-down NO emissions and tropospheric NO_2 columns from GEMS and model. Hourly variations in bottom-up and top-down NO emissions (left) and GEMS tropospheric NO_2 columns and model NO_2 columns (right) over major source regions during weekdays in the study period. Correlation coefficient and RMSE values are shown on the right panel. The unit of RMSE is 10^{15} molec cm^{-2}.

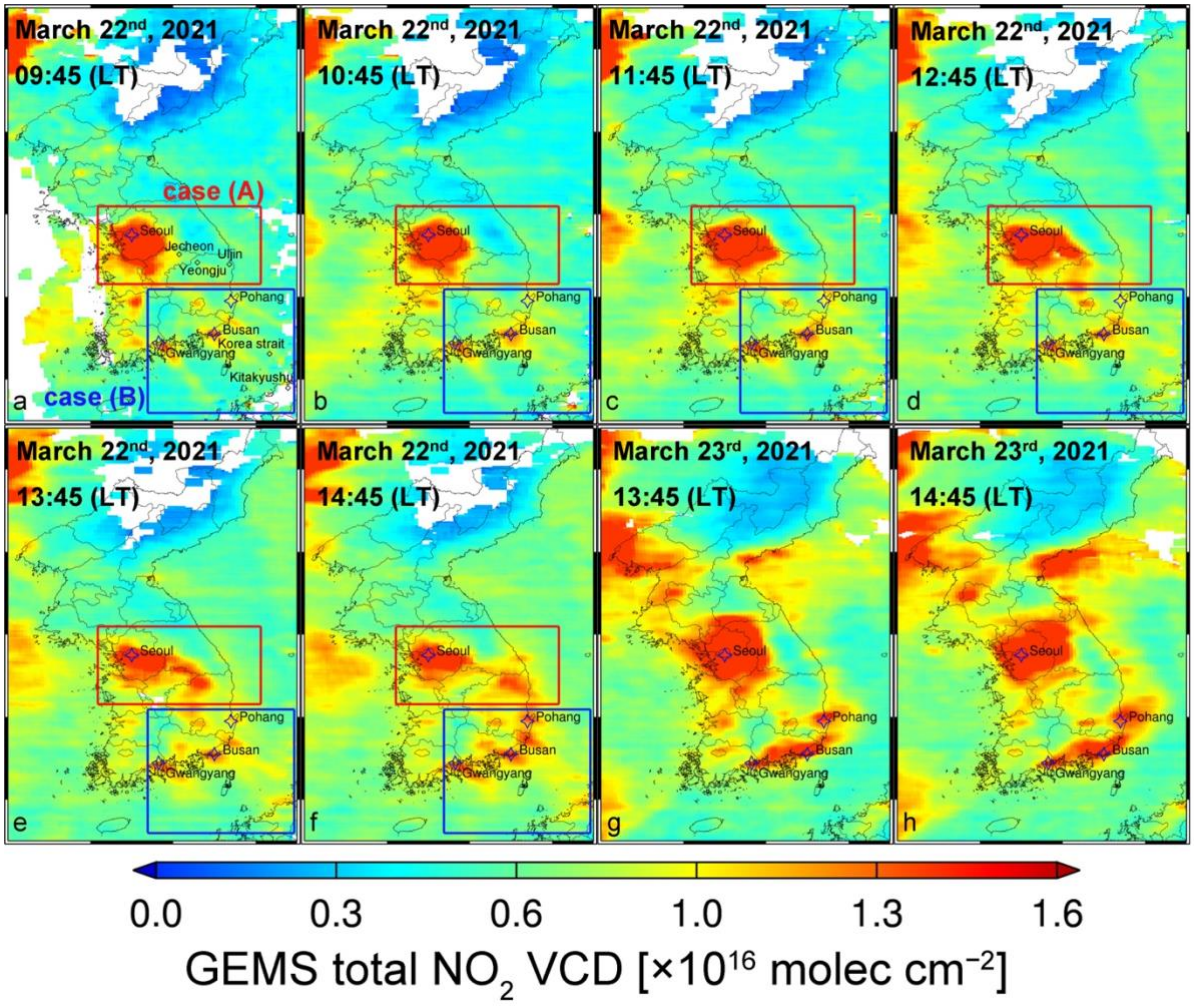

997

998 **Fig. 4. Transport of NO_2, revealed by GEMS hourly column analysis over the Korean**
999 **Peninsula, Korea Strait, and Japan.** a–f: Hourly GEMS NO_2 observations for 09:45–14:45
1000 LT, March 22, 2021. g and h: GEMS NO_2 observations for 13:45–14:45 LT, March 23, 2021
1001 (these panels represent a day without NO_2 long-range transport). Red and blue boxes indicated
1002 the regions for NO_2 transport case (A) and case (B), respectively.